A major purpose of the Technical Information Center is to provide the broadest dissemination possible of information contained in DOE's Research and Development Reports to business, industry, the academic community, and federal, state and local governments.

Although a small portion of this report is not reproducible, it is being made available to expedite the availability of information on the research discussed herein.

CONF-850254--1

Los Alamos National Laboratory is operated by the University of California for the United States Department of Energy under contract W-7405-ENG-36

LA-UR--84-4035

DE85 005562

TITLE KIVA: A COMPREHENSIVE MODEL FOR 2D and 3D ENGINE SIMULATIONS

AUTHOR(S) A. A. Amsden, T. D. Butler, P. J. O'Rourke, and J. D. Ramshaw

SUBMITTED TO SAE International Congress and Exhibition to be held
Feb. 27 - March 2, 1985, Detroit MI

Los Alamos National Laboratory
Los Alamos, New Mexico 87545

ABSTRACT

This paper summarizes a comprehensive numerical model that represents the spray dynamics, fluid flow, species transport, mixing, chemical reactions, and accompanying heat release that occur inside the cylinder of an internal combustion engine. The model is embodied in the KIVA computer code. The code calculates both two-dimensional (2D) and three-dimensional (3D) situations. It is an outgrowth of the earlier 2D CONCHAS-SPRAY computer program. Sample numerical calculations are presented to indicate the level of detail that is available from these simulations. These calculations are for a direct injection stratified charge engine with swirl. Both a 2D and a 3D example are shown.

I. INTRODUCTION

For some years we have been developing comprehensive numerical models to simulate the in-cylinder dynamics of advanced internal combustion engines. The first of these was the 2D RICE code (1,2)[a], which treated the premixed combustion of gaseous fuels in an enclosed bomb. This code was ably extended by Bracco and co-workers into the REC code (3), which treats quasi-3D dynamics by including the effects of piston motion. RICE was superseded by CONCHAS (4), which again treated gaseous combustion in 2D but with an arbitrary-Lagrangian-Eulerian (ALE) mesh (5) that permitted the piston shape and motion to be included naturally in the calculations. This code was followed by CONCHAS-SPRAY (6), which treated fuel sprays in the engine cylinder using the spray model developed by Dukowicz (7) and later extended by O'Rourke and Bracco (8) and O'Rourke (9). This paper summarizes the KIVA code (10), which treats the dynamics in either 2D or 3D with fuel sprays in arbitrary geometry.

The purposes of this paper are to describe the overall capabilities of KIVA, to briefly sketch the numerical procedures that are used to accomplish the solution, including more detail on those features that are significant improvements over CONCHAS-SPRAY, and to illustrate the use of the code with numerical examples. For specific details of the finite difference equations and their solution, the interested reader is referred to Ref. 10 and the references cited therein.

II. THE NUMERICAL MODEL

A. SUMMARY OF OVERALL CAPABILITIES — KIVA is a computer program which may be used to generate numerical solutions to multicomponent chemically reactive fluid flow problems. The program has been developed with applications to internal combustion engines specifically in mind, and it contains a number of features to facilitate such applications. Several engine concepts of current interest, in particular the diesel and direct-injection stratified-charge (DISC) engines, are of the fuel-injection type, so the capability to represent an evaporating fuel spray has been included.

KIVA is essentially a three-dimensional version of the earlier two-dimensional program CONCHAS-SPRAY. Aside from the dimensionality, the main differences in features between the two programs are the following: (a) KIVA uses an acoustic-subcycling method (11) for computer efficiency at low Mach number, instead of the pressure iteration used in CONCHAS-SPRAY; (b) the simple subgrid scale turbulence model used in CONCHAS-SPRAY has been generalized to include a transport equation for the turbulent kinetic energy associated with the subgrid scale motions; (c) the spray model used in

[a] Numbers in parentheses refer to references at end of paper.

CONCHAS-SPRAY has been augmented by a model for droplet collisions and coalescence (9), which have been found important in many typical applications; and (d) KIVA has been written for the CRAY computer and makes extensive use of the vector calculation feature of this computer. Because of these improvements and because KIVA can be easily specialized to planar and axisymmetric two-dimensional flows, it is intended that KIVA supersede CONCHAS-SPRAY.

KIVA is a time-marching program that solves finite-difference approximations to the governing differential equations. The transient solution is marched out in a sequence of finite time increments called cycles or time steps. Values of the dependent variables on each cycle are calculated from those on the previous cycle. The temporal difference scheme is explicit, with the use of an acoustic subcycling method (11) for efficiency at low Mach number.

Spatial differences are formed with respect to a generalized three-dimensional finite-difference mesh or grid, which subdivides the region of interest into a number of small cells or zones. The corners of the cells are called the vertices. The positions of the vertices may be arbitrarily specified as functions of time, thereby allowing a Lagrangian, Eulerian, or mixed description. Since the locations of the vertices are arbitrary, the cells are arbitrary hexahedrons. This type of mesh is called an ALE (arbitrary Lagrangian-Eulerian) mesh (5,12), and is particularly useful for representing curved and/or moving boundary surfaces. The spatial differencing is made conservative wherever possible. The procedure used is to difference the basic equations in integral form, with the volume of a typical cell used as the control volume, and the divergence terms transformed into surface integrals using the divergence theorem (5,13,14).

The effects of turbulence are represented by a generalized subgrid scale (SGS) turbulence model, whose use is optional. This model includes a transport equation for the turbulent kinetic energy associated with the subgrid scale motions. Boundary layer drag and heat transfer are calculated by matching to a modified turbulent law of the wall.

The numbers of species and chemical reactions that can be represented in KIVA are arbitrary; they are limited only by computer time and storage considerations. Chemical reactions are treated by a procedure that distinguishes between slow reactions, which proceed kinetically, and fast reactions, which are assumed to be in equilibrium (15,16). Chemical rate expressions for the kinetic reactions are evaluated by the same partially implicit procedure used in CONCHAS-SPRAY (6). The rate coefficients are assumed to be of a generalized Arrhenius form. The equilibrium reactions are treated by a new iterative procedure (16), which is an improvement over that used in CONCHAS-SPRAY.

Evaporating liquid sprays are represented by a discrete-particle technique (7), in which each computational particle represents a number of similar physical droplets. The radius and other attributes of a particle are statistically assigned using a Monte Carlo sampling technique. The particles and fluid interact by exchanging mass, momentum, and energy. These interactions are treated by implicit coupling procedures to avoid the prohibitively small time steps that would otherwise often be necessary. Turbulence effects on the droplets are accounted for by adding a fluctuating component to the local mean gas velocity when calculating each particle's mass, momentum, and energy exchange with the gas (7). Droplet collisions and coalescence are accounted for, but the spray is otherwise assumed to be thin; volume-displacement (7) and other thick-spray effects (9) are neglected.

B. GEOMETRY AND GENERALIZED MESH — The spatial differencing is based on the ALE method (5,12), which in three dimensions uses a mesh made up of arbitrary hexahedrons. Spatial difference approximations are constructed by the control-volume or integral-balance approach (5,13,14), which largely preserves the local conservation properties of the differential equations.

Together, the cells constitute the mesh with respect to which spatial differences are formed. The vertices need not be stationary, but may move in an arbitrarily prescribed manner. This capability includes the Lagrangian and Eulerian descriptions as special cases. In the general case, the cells are asymmetrical; a typical cell is shown in Fig. 1. The vertices are conventionally numbered as shown.

The cells are indexed by integers (i,j,k), which may be regarded as coordinates in logical space. The indices (i,j,k) also label the vertices, with the understanding that vertex (i,j,k) is vertex 4 of cell (i,j,k). The Cartesian coordinates of vertex (i,j,k) are $(x_{ijk}, y_{ijk}, z_{ijk})$, which in general depend on the time t.

A generalized mesh of the ALE type provides a great deal of geometrical flexibility. It allows a convenient direct representation of curved and moving boundaries, such as a moving cupped piston. The geometrical flexibility is illustrated in Fig. 2, which shows the outline of a mesh used to represent an engine cylinder with an offset-bowl cupped piston design. This type of mesh is a wrap-around mesh formed as shown in Fig. 3. The other mesh options available in KIVA are shown in Fig. 4. These include both planar and cylindrical geometries for 2D calculations, and an unwrapped 3D mesh as shown in the lower left of the figure. In the latter case, in general, the cells need not be square or rectangular, so a variety of different geometries can be represented by distorting the cells and deactivating other cells to form obstacles. An

unwrapped mesh representation of an engine cylinder with valves is shown in Fig. 3.

C. TURBULENCE MODEL — The turbulence model used in KIVA is a subgrid scale transport model which is a natural generalization of the original algebraic subgrid scale model used by Smagorinsky (17), Deardorff (18,19), and others. The generalization consists in the introduction of a new dependent variable q that represents the kinetic energy per unit mass of the turbulent length scales that are too small to resolve in the mesh. The variable q satisfies a transport equation which contains production and decay terms and terms representing the convection and self-diffusion of the turbulence. This equation takes the form

$$\frac{\partial}{\partial t}(\rho q) + \nabla\cdot(\rho q \underline{u}) = -\frac{2}{3}\rho q \nabla\cdot\underline{u} + \underline{\underline{g}}:\nabla\underline{u} + \nabla\cdot(\mu\nabla q) - \hat{D}\rho L^{-1}q^{3/2} + \dot{W}_g \quad , \qquad (1)$$

where ρ is the fluid density, $\underline{\underline{g}}$ is the turbulent stress tensor, μ is the turbulent viscosity, D is a constant of order unity, L is a characteristic length on the order of twice the mesh spacing, and $\dot{W}_g$ is a source term representing the production of turbulence by the motion of the fuel spray droplets through the gas. The turbulent viscosity is given in terms of q by $\mu = A\rho L q^{1/2}$, where A = 0.05, and $\underline{\underline{g}}$ is related to μ by the usual Newtonian stress law.

The physical meaning of the various terms is as follows. The term $\nabla\cdot(\rho q\underline{u})$ simply represents convection of the turbulence by the resolved velocity field. The term $-(2/3)\rho q\nabla\cdot\underline{u}$ is a compressibility term that represents the turbulent analog of pdV work. The term $\underline{\underline{g}}:\nabla\underline{u}$ represents the production of turbulence by shear in the resolved velocity field, and $\nabla\cdot(\mu\nabla q)$ represents the self-diffusion of the turbulence with a diffusivity of μ/ρ. The term $-\hat{D}\rho L^{-1}q^{3/2}$ represents the decay of turbulent energy into thermal energy. This term appears with the opposite sign as a source term in the thermal internal energy equation, in place of the term $\underline{\underline{g}}:\nabla\underline{u}$. The term $\underline{\underline{g}}:\nabla\underline{u}$ may also be looked upon as the rate at which kinetic energy of the resolved motions is dissipated by the turbulence. If q were not retained as a variable this energy would have to be considered as being converted directly to thermal energy, and the term $\underline{\underline{g}}:\nabla\underline{u}$ would then appear in the thermal energy equation. Here, however, the dissipated kinetic energy is regarded as being converted first into q, so that the term $\underline{\underline{g}}:\nabla\underline{u}$ is removed from the thermal energy equation and put into the q equation instead. The rate of final conversion to thermal energy is $\hat{D}\rho L^{-1}q^{3/2}$, so this term replaces $\underline{\underline{g}}:\nabla\underline{u}$ in the thermal energy equation. Thus the physical picture is that the kinetic energy of the resolved velocity field is not dissipated directly to heat by the action of $\underline{\underline{g}}$, but is first converted into subgrid scale turbulent energy q, which is ultimately converted to heat by the decay term $\hat{D}\rho L^{-1}q^{3/2}$.

It is of interest to note that in the quasi-steady situation where the production and decay terms balance, the above model reduces to the original algebraic subgrid scale model. Equating production and decay, we obtain, with D = 1,

$$\underline{\underline{g}}:\nabla\underline{u} = \rho L^{-1}q^{3/2} \quad . \qquad (2)$$

Assuming incompressible flow for simplicity, we have that $\underline{\underline{g}} = \mu[\nabla\underline{u} + (\nabla\underline{u})^T]$, where superscript T denotes the transpose. Furthermore, $q^{3/2} = (\mu/A\rho L)^3$. We thereby obtain

$$(\mu/\rho)^2 = \frac{1}{2}A^3L^4\underline{\underline{D}}:\underline{\underline{D}} \qquad (3)$$

or

$$\mu = \frac{1}{\sqrt{2}}\rho A^{3/2}L^2(\underline{\underline{D}}:\underline{\underline{D}})^{1/2} \quad , \qquad (4)$$

where $\underline{\underline{D}} = \nabla\underline{u} + \nabla\underline{u}^T$. This is of exactly the same form as the original algebraic subgrid scale eddy viscosity (19), and provides a relation between the coefficient A and the original algebraic subgrid scale coefficient C (19). Using $L = 2\Delta x$, this relation is found to be $C^2 = 4A^{3/2}$, or $C = 2A^{3/4}$. It is known (19) that C ~ 0.2, which implies the value A ~ 0.05 mentioned above. Thus the present subgrid scale transport model includes the earlier algebraic model as a special case.

D. SUBCYCLING, PRESSURE GRADIENT SCALING, AND ACOUSTIC DAMPING — Numerical calculations of compressible fluid flow have a notorious tendency to be inefficient at low Mach numbers because of the wide disparity between the time scales associated with convection and the propagation of sound waves. In explicit schemes, this inefficiency occurs because the time steps needed to satisfy the sound-speed stability condition are much smaller than those needed to satisfy the convective stability condition alone. In implicit schemes the inefficiency manifests itself in the additional computational labor needed to solve the implicit system of equations on each time step. This solution is usually performed by iterative techniques.

Provided that the Mach number is not too low, there is a third alternative which effectively combines the advantages of explicit

and implicit methods while largely avoiding the disadvantages. This is the acoustic subcycling method (11), in which all terms in the governing equations that are not associated with sound waves are explicitly advanced with a relatively large time step Δt similar to that of an iterative method. The terms associated with acoustic waves (namely the compression terms in the continuity and energy equations and the pressure gradient in the momentum equation) are explicitly advanced using a smaller time step δt that satisfies the sound-speed stability condition and of which the main time step Δt is an integral multiple. This method eliminates much of the inefficiency of a purely explicit scheme while preserving the simplicity and robustness thereof. The subcycling plays a role analogous to the iteration in implicit methods, but unlike the latter it has the advantage that it is not open-ended. That is, the number of subcycles is fixed by the ratio of stability limits and cannot become unreasonably large, as the number of iterations frequently does.

The acoustic subcycling method works very well in most internal combustion engine calculations, where the Mach numbers are not unduly low. The primary disadvantage of the method is that it is unsuitable for very low Mach numbers, such as those that occur in an engine cylinder at very low RPM. The problem is simply that the number of subcycles $N = \Delta t/\delta t$ tends to infinity as the Mach number tends to zero, and once N exceeds 50 or so an implicit scheme becomes more efficient. To extend the applicability of the method to lower Mach numbers, we combine it with the pressure gradient scaling (PGS) method (20).

Pressure gradient scaling is a method for artificially increasing the Mach number to somewhat larger values while still keeping it small in an absolute sense. This is done by multiplying the pressure gradient in the momentum equation by a time-dependent scaling factor $1/\alpha^2(t)$, where $\alpha(t) > 1$. One readily verifies that this modification has the desired effect of reducing the effective sound speed by a factor of α. However, it might at first be expected to affect the solution in other ways as well, and therefore to be unacceptable. In particular, since the pressure gradient has no way of distinguishing pressure inhomogeneities of acoustic origin from any other pressure inhomogeneities, one might expect to incur errors in accelerations, and hence in velocities, that are not merely acoustic in character. Fortunately, and perhaps surprisingly, this fear is not well founded. Physically, the saving grace is that the pressure gradients in a low Mach number flow are effectively determined by the velocity field, and not vice versa. The pressure gradients adjust themselves to whatever values are necessary for the velocity field to have the correct divergence (which in general is nonzero) (21,22). The presence of the factor $1/\alpha^2$ merely causes these gradients to become larger by a factor of α^2 in order to establish the same velocity field.

The preceding remarks do not, of course, provide a firm justification for the PGS method; they are merely a plausibility argument. A systematic derivation of the method is presented in Ref. 20. This derivation shows that the basic condition for the PGS method to be applicable is not that the Mach number be low per se, but rather that pressure inhomogeneities be negligible. Ordinarily, of course, these two conditions are closely related (22), but the latter is really the more fundamental in the present context.

Within the context of the acoustic subcycling method, the PGS method improves numerical efficiency by reducing the number of subcycles required. Reduction of the sound speed by a factor of α allows δt to be increased by the same factor, and thus the number of subcycles $N = \Delta t/\delta t$ is reduced by a factor of α. The appropriate value of α is automatically selected in an adaptive manner by continually monitoring the magnitude of the pressure inhomogeneities that occur in the calculation. If these inhomogeneities are smaller than a specified tolerance that the user considers "essentially uniform pressure" then the value of α is increased. If the pressure inhomogeneities become large enough that the pressure field threatens to become sensibly nonuniform then α is decreased. The details of the algorithm for the automatic selection of α are given in Ref. 20.

The acoustic subcycling and PGS methods are used in conjunction with a procedure for damping sound waves. The sound waves are not themselves of interest in low Mach number combustion problems, but in some cases they can distract attention from or even conceal other flow features that are of interest, especially in velocity vector plots at a fixed instant of time. This danger is increased by the PGS method, which artificially increases the amplitude of the sound waves in the process of artificially reducing their speed. Implicit schemes frequently contain sufficient intrinsic damping to eliminate unwanted sound waves, but the acoustic subcycling method is neutrally stable and has no intrinsic damping of its own. We therefore introduce an acoustic damping term into the KIVA subcycling procedure. The effect of this term is roughly comparable to that provided by the truncation errors in typical implicit schemes. This term takes the form of an artificial pressure p^* defined by

$$p^* = -\rho_0^* \rho c^2 \delta t[\nabla\cdot\underline{u} - (\nabla\cdot\underline{u})_0] \quad , \qquad (5)$$

where ρ_0^* is a user-specified coefficient of order unity, c is the sound speed, $\underline{u}$ is the fluid velocity, and $(\nabla\cdot\underline{u})_0$ is the velocity di-

vergence that would obtain in the limit of zero Mach number ($c \to \infty$). The presence of $(\nabla \cdot \underline{u})_0$ is essential, as otherwise the damping would not be confined to the sound waves alone. The value of $(\nabla \cdot \underline{u})_0$ is determined by the boundary conditions, the rate of chemical heat release, and the rates of heat conduction and viscous dissipation (21,22). The artificial pressure p^* is added to the thermodynamic pressure p during the subcycling.

The value of $p_0^* = 1/2$ corresponds roughly to the same amount of acoustic damping as that of the implicit scheme used in CONCHAS-SPRAY (6), if the implicit scheme were run with a time step of δt. Ordinarily, of course, the implicit scheme will use a substantially larger time step and will therefore have additional acoustic damping. The value of p_0^* cannot in general be increased to match the acoustic damping of an implicit scheme, because stability considerations limit the maximum allowed p_0^* to values on the order of unity.

It may be noted that in problems without significant heat release $\nabla \cdot \underline{u}_0$ is often essentially uniform and the use of p^* is then simply equivalent to an artificial bulk viscosity $p_0^* \rho c^2 \delta t$. A fuller discussion of the present acoustic damping method will be given elsewhere (23).

E. SPRAY MODEL — The dynamics of atomized fuel sprays are represented by a Monte Carlo based discrete-particle technique (7). The spray is considered to be composed of discrete computational particles, each of which represents a group of droplets of similar physical properties. The distribution function in droplet size, velocity, spray pattern, and temperature produced by the fuel injector is statistically sampled and the resulting Lagrangian particles are followed as they locally interact and exchange mass, momentum, and energy with the gas. The model accounts for turbulence effects (7) and interactions between droplets (9), but other thick spray effects are neglected.

Extensions of this model over those reported in Ref. 6 are the inclusion of the droplet-droplet interaction model and a new procedure for sampling the distribution functions that requires fewer computational particles to achieve good statistics for the spray dynamics. Details of the droplet collision model are too involved to describe here; the interested reader is referred to Refs. 9 and 10.

Very briefly, drop collisions themselves are calculated by a sampling procedure. We calculate the collision frequency and use this frequency in determining the probability that a drop in the given particle will undergo a collision with a drop in a nearby particle. Then all drops in the given particle behave in the same manner; they either do or do not collide, and no new computational particles are created. This procedure has proven preferable to a more straightforward alternative whereby the collision frequency is used to determine the probable number of drops in a given particle that will have collisions with drops in another particle; one or more new particles are then created having the properties of the drops resulting from the collisions. We tried the latter procedure and found that we very soon had more computational particles in a typical application than could be accommodated by computer storage. In the former procedure the probability distribution of outcomes is recovered by ensemble averaging over many computations, or, in a steady state calculation, by long time averaging.

Particles are introduced into the computational mesh in such a way that a specified distribution of drop sizes is obtained. The method we have chosen for this samples those portions of the specified drop-size distribution most frequently where the most drop mass occurs. This is motivated by the assumption that these drops will usually exchange the largest amounts of mass, momentum, and energy with the gas. This procedure has proven very beneficial, especially in 3D applications, by limiting the number of computational particles required to achieve statistical independence of the number of particles in the spray.

Two distributions are associated with the injection calculation. Occurrence of the drop radius r at injection is governed by the probability distribution f(r). We define another distribution g(r) in such a way that g(r)dr is the probability that a particle has drops with radii in the range (r, r + dr). The number of drops per particle is then proportional to the ratio f(r)/g(r). Best resolution of the drop size distribution is obtained where the values of g(r) are largest, and to obtain the best resolution of the size distribution where the most drop mass is located, g(r) should be proportional to the mass distribution $r^3 f(r)$, assuming that all liquid has the same mass density. Thus, the number of drops per particle is proportional to $1/r^3$. From this it follows that the total droplet mass associated with each particle is constant. This constant is determined by dividing the total spray mass to be injected by the total number of particles to be injected. So the total number of particles to represent the spray event is given *a priori*.

III. NUMERICAL EXAMPLES

To illustrate KIVA's capabilities, we present two numerical examples. These are a 2D and a 3D simulation of the in-cylinder dynamics of a DISC engine. The simulations follow the dynamics through the compression, fuel injection, ignition, and burn phases of the cycle. The 2D calculation is axisymmetric and the 3D calculation is similar in all respects

until the ignition event. In 3D, ignition is from two locations in the cylinder instead of the "ring" ignition, which is necessary in 2D to represent off-axis ignition. Figure 6 shows the outline of the 3D computing mesh at 90° BTDC, when the calculation begins. The mesh is composed of 20 cells radially by 24 cells azimuthally by 22 cells axially. The 2D mesh has the same radial and axial resolution as its 3D counterpart. At this time, the cylinder contains only pure air in rigid body swirl, with a swirl ratio of 3. The engine is operating at 1600 rpm.

During the compression stroke, liquid octane fuel is sprayed into the cylinder from a single-pulse injector on the cylinder axis. The injection begins at 52° BTDC and ends at 39.3° BTDC, supplying 11.6 mg of fuel in the form of a 75° hollow cone spray. The overall equivalence ratio is 0.27. Figure 7 shows selected plots just prior to ignition of the fuel-air mixture at 27° BTDC for the 3D case. Although 2000 computational particles (each representing some number of identical physical droplets) have been injected, evaporation and coalescence have reduced their number to only 747 particles at this time. Also evident in Fig. 7 is the effect of spray drag on the velocity field, and a cool region in the temperature field due to spray evaporation. The turbulent kinetic energy contours are quite symmetric, with the high values concentrated on the axis. The fuel cloud is centered in the bowl and well away from the walls. The spark locations are based on consideration of the equivalence ratio contours at this time. Ideally, ignition should be located where $\phi = 1$ (Fig. 7).

Chemically, we represent this problem using 12 species among which occur four kinetic reactions and six equilibrium reactions. The kinetic reactions are:

$$2C_8H_{18} + 25O_2 \rightarrow 16CO_2 + 18H_2O \quad ,$$

$$O + N_2 \rightleftharpoons NO + N \quad ,$$

$$O_2 + N \rightleftharpoons NO + O \quad ,$$

$$OH + N \rightleftharpoons NO + H \quad .$$

The first reaction is a single-step octane oxidation reaction, and the next three reactions represent the extended Zel'dovich mechanism for NO production.

The equilibrium reactions are

$$N_2 \rightleftharpoons 2N \quad ,$$

$$O_2 \rightleftharpoons 2O \quad ,$$

$$N_2 \rightleftharpoons 2N \quad ,$$

$$O_2 + N_2 \rightleftharpoons 2OH \quad ,$$

$$O_2 + 2H_2O \rightleftharpoons 4OH \quad ,$$

$$O_2 + 2CO \rightleftharpoons 2CO_2 \quad .$$

Figure 8 shows selected views at 20° BTDC, 7° after ignition. Temperature contours are shown through two planes passing through the spark locations, and indicate that the flame region on the left is slightly larger than the one on the right. This three-dimensional effect results from the stochastic nature of the spray model. The plot of octane mass fraction indicates the two regions where the nearly spherical flames have begun to deplete the rich fuel cloud.

Figure 9 shows velocity and temperature at 0° (TDC), again through the plane of the spark plugs for contrast with the previous figure. The two flames have now merged, and their separate effects have been swept around by the swirl to such an extent that the overall flow has regained its circular symmetry to a remarkable degree. The fuel vapor, which began to burn significantly at about 20° BTDC, is being consumed at a rapid rate at TDC.

Figure 10 is a summary graph of the fuel in the engine cylinder as a function of crank angle during the cycle. Both the liquid and vapor phases are shown. The plots are essentially the same for the 2D and the 3D simulations until just after ignition when the 3D case indicates an initially faster burn rate. The main reason for this difference is the increased turbulent kinetic energy induced by the burning from the two spark locations in 3D. This can be seen in Fig. 11, in which are plotted contours of turbulent kinetic energy for the 2D and 3D cases at 14° BTDC. The 3D values are an order of magnitude higher than for the 2D case and are located near the axis. The high values for the 2D case are located near the top of the piston bowl in the squish region. The 3D contours show essentially the same numerical values as the 2D case in this region, indicating that the increase along the axis is due to the burning from the merging flame kernels. Subsequently, the burn rate in 2D catches and surpasses that in the 3D case. By TDC values of the turbulent kinetic energy in the vicinity of the flame are essentially equal for the two cases.

The conditions for these examples are typical for DISC engine operation, but no attempt has been made to optimize the cylinder geometry or other engine parameters for efficient operation.

Acknowledgement

We are most grateful to L. D. Cloutman for his efforts in performing the 3D calculation. This work was supported by the Combustion Technology Program of the United States Department of Energy.

REFERENCES

1. W. C. Rivard, O. A. Farmer, and T. D. Butler, "RICE: A Computer Program for Multicomponent Chemically Reactive Flows at All Speeds," Los Alamos Scientific Laboratory report LA-5812 (1975).

2. T. D. Butler and P. J. O'Rourke, Sixteenth Symposium (International) on Combustion, Combustion Institute, Pittsburgh, 1503 (1976).

3. H. C. Gupta and S. A. Syed, "REC-P3 (Reciprocating Engine Combustion, Planar Geometry, Third Version): A Computer Program for Combustion in Reciprocating Engines," MAE Report No. 1431, Mechanical and Aerospace Engineering Department, Princeton University (1979).

4. T. D. Butler, L. D. Cloutman, J. K. Dukowicz, and J. D. Ramshaw, "COMCHAS: An Arbitrary Lagrangian-Eulerian Computer Code for Multicomponent Chemically Reactive Fluid Flow at All Speeds," Los Alamos Scientific Laboratory report LA-8129-MS (November 1979).

5. C. W. Hirt, A. A. Amsden, and J. L. Cook, J. Comput. Phys. 14, 227 (1974).

6. L. D. Cloutman, J. K. Dukowicz, J. D. Ramshaw, and A. A. Amsden, "COMCHAS-SPRAY: A Computer Code for Reactive Flows with Fuel Sprays," Los Alamos National Laboratory report LA-9294-MS (May 1982).

7. J. K. Dukowicz, J. Comput. Phys. 35, 229 (1980).

8. P. J. O'Rourke and F. V. Bracco, "Modelling of Drop Interactions in Thick Sprays and a Comparison with Experiments," Institution of Mechanical Engineers Paper C404/80.

9. P. J. O'Rourke, "Collective Drop Effects in Vaporizing Liquid Sprays," Ph.D. Thesis, Princeton University, and Los Alamos National Laboratory report LA-9069-T (November 1981).

10. A. A. Amsden, J. D. Ramshaw, P. J. O'Rourke, and J. K. Dukowicz, "KIVA: A Computer Program for Two- and Three-Dimensional Fluid Flows with Chemical Reactions and Fuel Sprays," Los Alamos National Laboratory report LA-10245-MS (1985).

11. L. C. Haselman, "TDC—A Computer Code for Calculating Chemically Reacting Hydrodynamic Flows in Two Dimensions," Lawrence Livermore Laboratory report UCRL-52931 (22 May 1980).

12. W. E. Pracht, J. Comput. Phys. 17, 132 (1975).

13. L. R. Stein, R. A. Gentry, and C. W. Hirt, Comp. Meth. Appl. Mech. Eng. 11, 57 (1977).

14. J. H. Tunstall, "On the Derivation of Conservative Finite-Difference Expressions for the Navier-Stokes Equations," Union Carbide Corporation, Nuclear Division report K/CSD-5, Oak Ridge, Tenn. (April 1977).

15. J. D. Ramshaw, Phys. Fluids 23, 675 (1980).

16. J. D. Ramshaw and A. A. Amsden, "Improved Iteration Scheme for Partial Equilibrium Flow," J. Comput. Phys. (accepted).

17. J. S. Smagorinsky, Month. Weather Rev. 91, 99 (1963).

18. J. W. Deardorff, J. Fluid Mech. 41, 453 (1970).

19. J. W. Deardorff, J. Comput. Phys. 7, 120 (1971).

20. J. D. Ramshaw, P. J. O'Rourke, and L. R. Stein, "Pressure Gradient Scaling Method for Fluid Flow with Nearly Uniform Pressure," J. Comput. Phys. (accepted).

21. J. D. Ramshaw and J. A. Trapp, J. Comput. Phys. 21, 438 (1976).

22. P. J. O'Rourke and F. V. Bracco, J. Comput. Phys. 33, 185 (1979).

23. J. D. Ramshaw, P. J. O'Rourke, and A. A. Amsden, "Acoustic Damping for Explicit Calculations of Fluid Flow at Low Mach Number," manuscript in preparation.

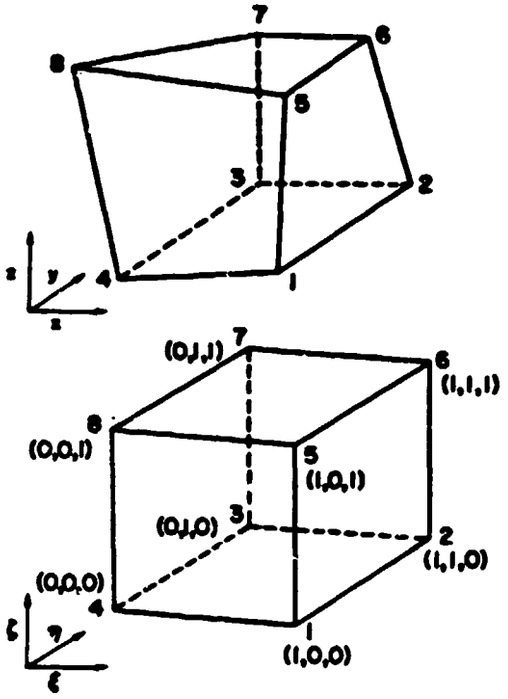

Fig. 1 - Relationship of a computational cell in physical (x,y,z) space to the unit cube in logical (ξ,η,ζ) space. KIVA vertex numbering is indicated.

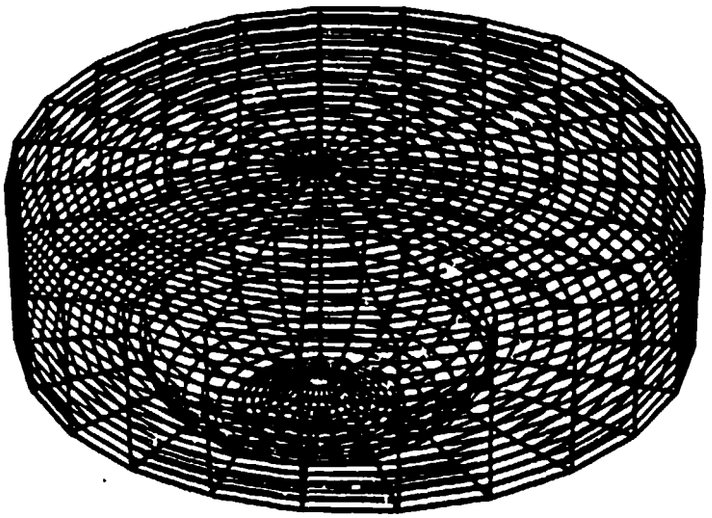

Fig. 2 - Outline of a KIVA computing mesh used to represent a diesel engine cylinder with an offset-bowl cupped piston.

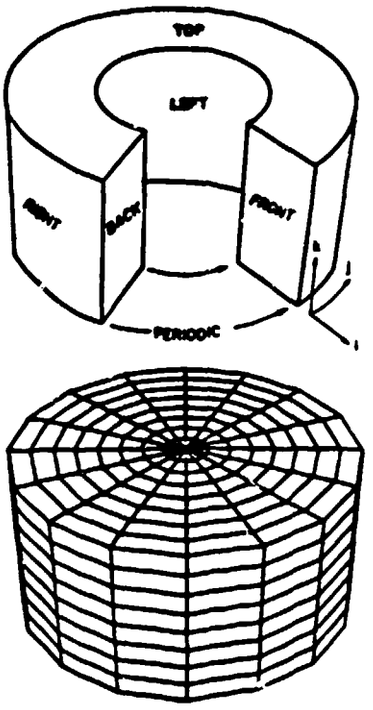

Fig. 3 - The KIVA 3D pseudo-polar grid formed from a Cartesian block of cells through the use of periodic boundary conditions.

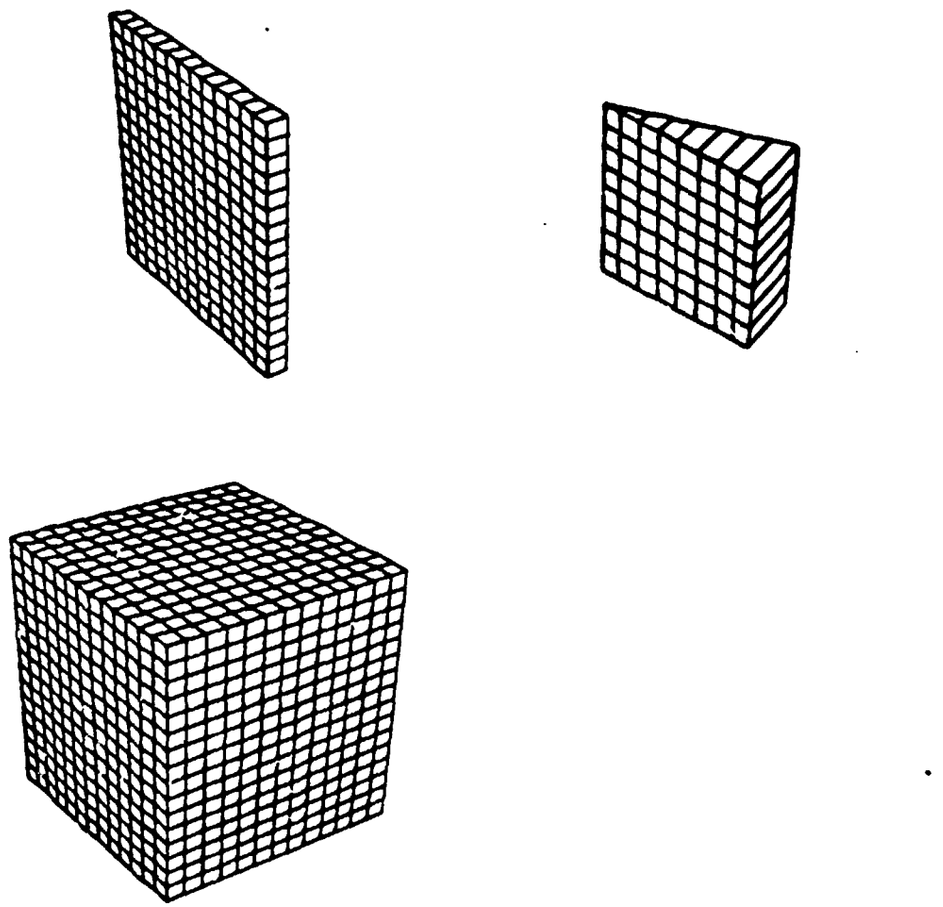

Fig. 4 - Other KIVA mesh options including both planar and cylindrical coordinates for 2D calculations, and an unwrapped 3D planar mesh.

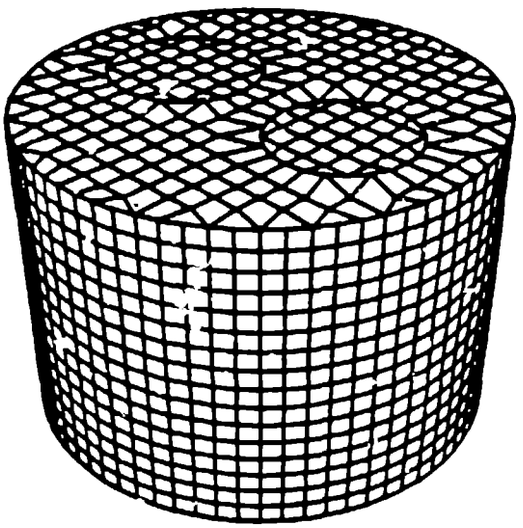

Fig. 5 - An unwrapped 3D mesh representation of an engine cylinder with valves in the head.

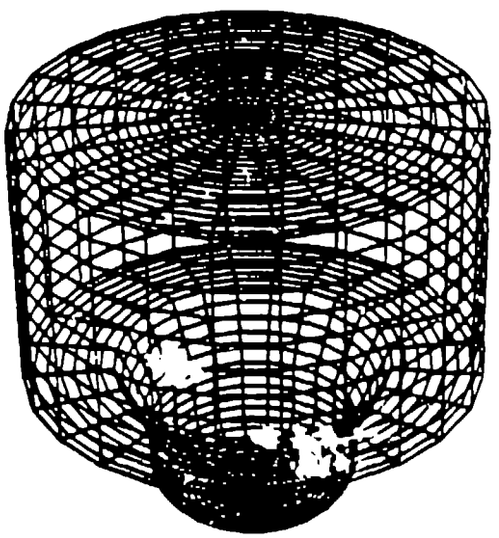

Fig. 6 - The computational mesh for the 3D example calculation at 90° BTDC.

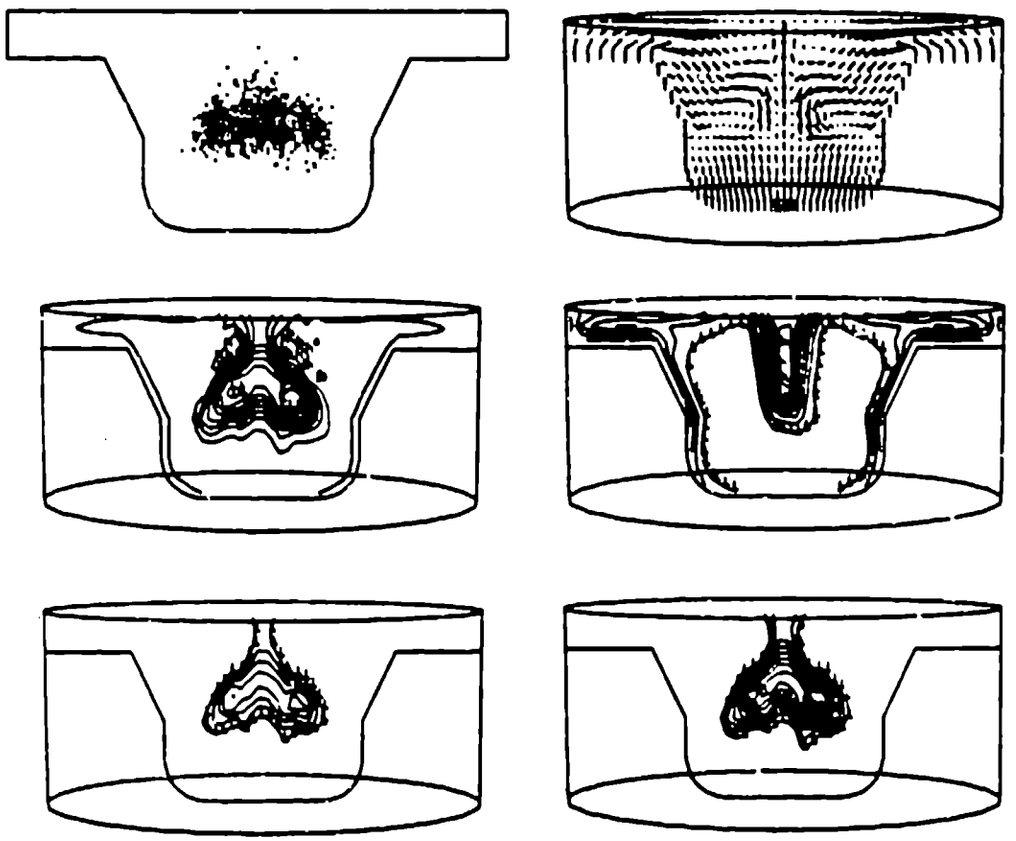

Fig. 7 - Selected views at 28° BTDC, just prior to ignition. Reading across, from top to bottom: The first plot shows the 747 spray droplets. The second plot shows velocity vectors; the maximum axial component is 932 cm/s. The third plot shows isotherms. The h contour is 680 K, the Δ contour is 495 K, and the contour interval is 23 K. The fourth plot shows turbulent kinetic energy. The h contour is 2.63×10^3 cm^2/s^2, the Δ contour is 3.18×10^4 cm^2/s^2. The fifth plot shows equivalence ratio. The maximum and minimum values are 2.64 and zero, the Δ contour and the contour interval are both 0.50. The last plot shows octane mass fraction. The maximum and minimum values are 0.142 and zero. The h contour is 0.127, and the Δ contour and the contour interval are both 0.014.

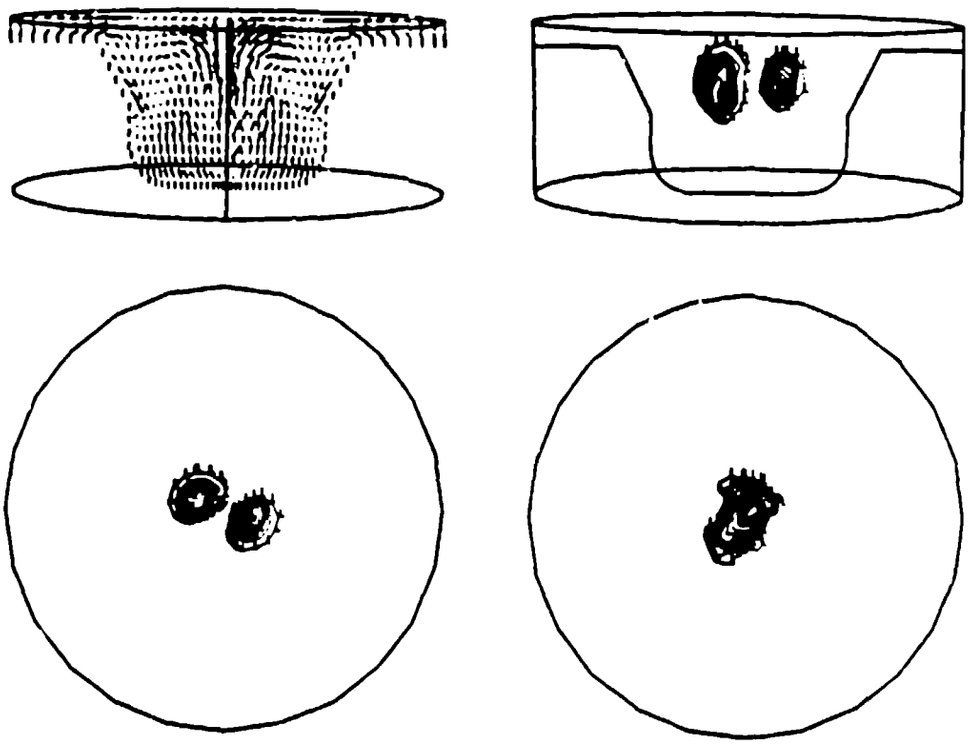

Fig. 8 - Selected views at 20° BTDC, 7° after ignition. Upper left: velocity vectors in the plane normal to the plane of the two spark locations. The maximum axial component is 1120 cm/s. Upper right: isotherms through the plane of the two spark locations. The h contour is 2205 K, the A contour is 767 K, and the contour interval is 180 K. The two lower views are overhead views through the ignition plane. On the left are isotherms. The h contour is 2386 K, the A contour is 799 K, and the contour interval is 198 K. On the right is the octane mass fraction. The h contour is 0.004, and the A contour and contour interval are 0.009.

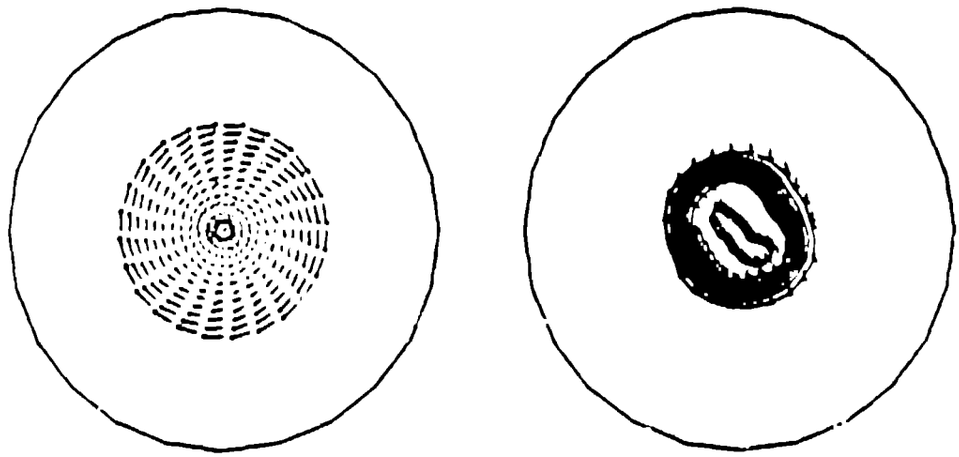

Fig. 9 - Overhead views at TDC, again through the ignition plane. On the left are velocity vectors, with a maximum swirl velocity of 3610 cm/s. On the right are isotherms. The h contour is 2466 K, the k contour is 1004 K, and the contour interval is 183 K.

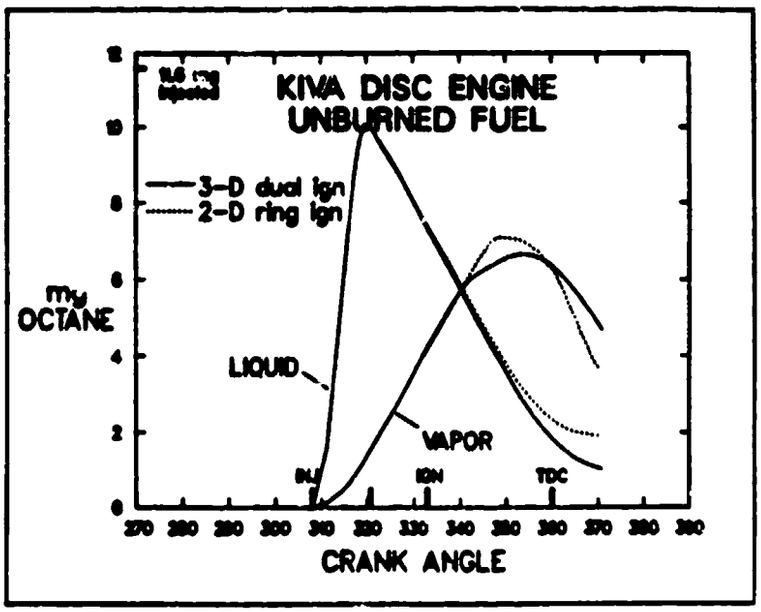

Fig. 10 - Unburned fuel in the cylinder as a function of crank angle.

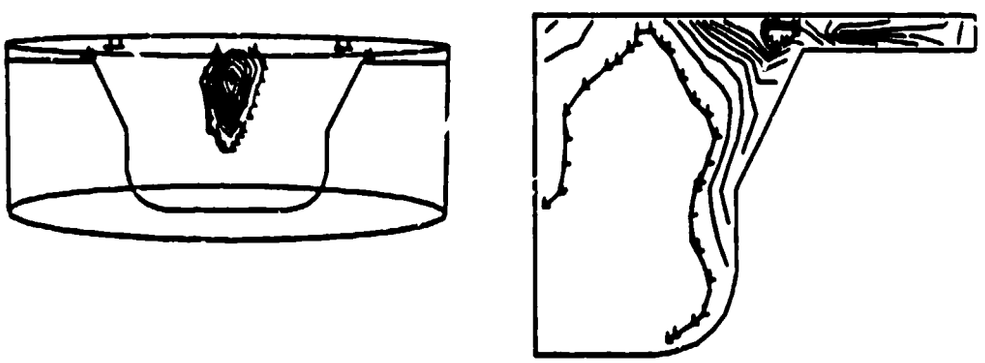

Fig. 11. - Turbulent kinetic energy at 14° BTDC. The plot on the left is from the 3D calculation. The h contour is 3.88×10^6 cm^2/s^2, the l contour is 4.39×10^5 cm^2/s^2, and the contour interval is 4.30×10^5 cm^2/s^2. The plot on the right is from the 2D calculation. The h contour is 5.23×10^5 cm^2/s^2, the l contour is 6.33×10^4 cm^2/s^2, and the contour interval is 5.74×10^4 cm^2/s^2.